iScience

CellPress
OPEN ACCESS

Article

A robust thin-film droplet-induced electricity generator

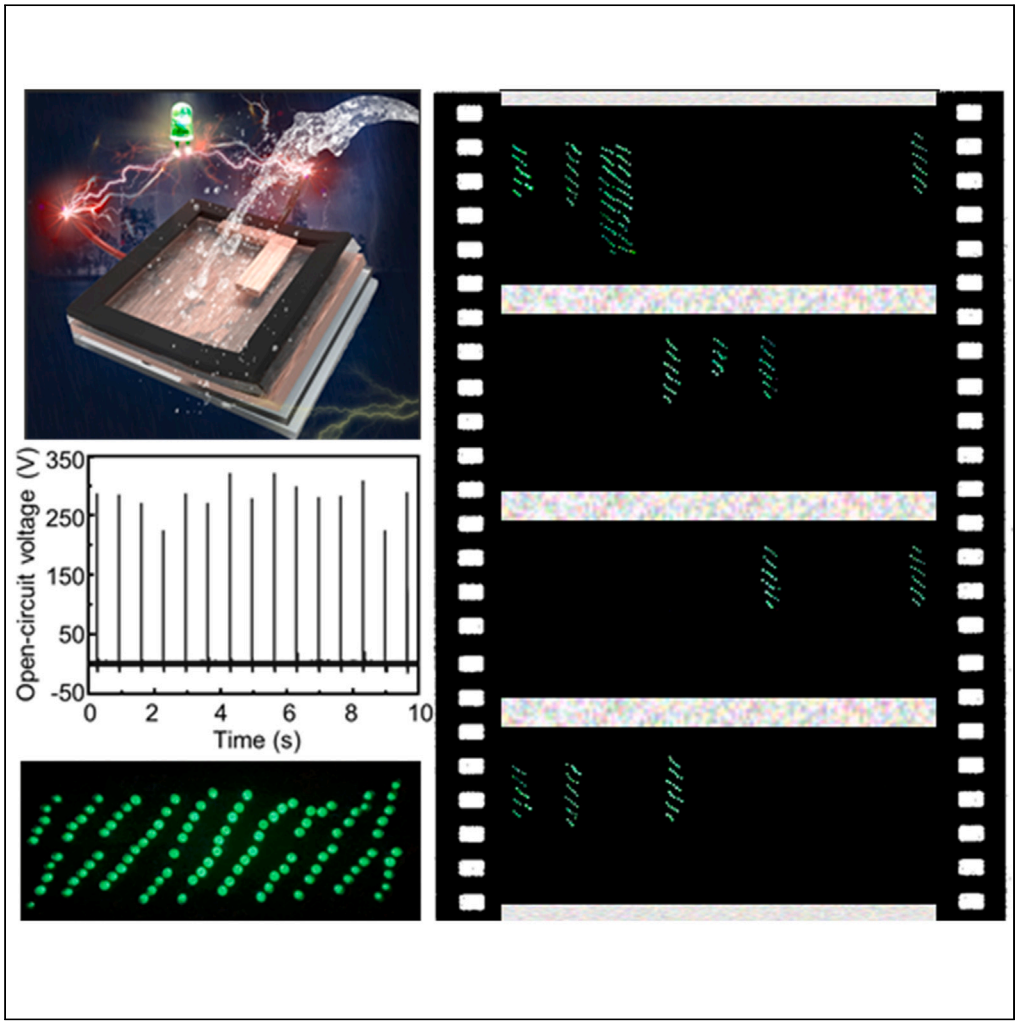

Haomin Song, Zongmin Bei, Aleksandr S. Voronin, ..., Udo Schwingenschlögl, Johannes S. Vrouwenvelder, Qiaoqiang Gan

qiaoqiang.gan@kaust.edu.sa

Highlights

Craft droplet generators economically without specialized cleanroom facilities

A thorough investigation into voltage-limiting factors

Achieved substantial open-circuit voltage enhancement, reaching 282.2 ± 27.9 V

Ten devices showcase diverse luminous LED patterns, emphasizing practical potential

Song et al., iScience *27*, 109291
March 15, 2024
https://doi.org/10.1016/j.isci.2024.109291

iScience

CellPress
OPEN ACCESS

Article

A robust thin-film droplet-induced electricity generator

Haomin Song,[1,7] Zongmin Bei,[2,3,7] Aleksandr S. Voronin,[4] Uma Pratheebha Umaiya Kunjaram,[3] Tadd T. Truscott,[5] Udo Schwingenschlögl,[4] Johannes S. Vrouwenvelder,[6] and Qiaoqiang Gan[1,3,8,*]

SUMMARY

The pursuit of cost-effective, high-voltage electricity generators activated by droplets represents a new frontier in hydropower technology. This study presents an economical method for crafting droplet generators using common materials such as solid polytetrafluoroethylene (PTFE) films and readily available tapes, eliminating the need for specialized cleanroom facilities. A thorough investigation into voltage-limiting factors, encompassing device capacitance and induced electrode charges, reveals specific areas with potential for optimization. A substantial enhancement in the open-circuit voltage (V_{oc}) was achieved, reaching approximately 282.2 $\pm$ 27.9 V—an impressive increase of around 60 V compared to earlier benchmarks. One device showcased its capability to power 100 LEDs concurrently, underscoring its efficacy. Ten such devices created diverse luminous patterns with uniform light intensity for each LED, showcasing the practical potential of the approach. The methodology's cost-effectiveness results in a remarkable cost reduction compared to solution-based materials, paving the way for the widespread adoption of large-scale water droplet energy harvesting.

INTRODUCTION

Given the scarcity of fossil fuels, the challenges associated with global warming, and the occurrence of climate anomalies, researchers are actively involved in advancing the transition toward low-carbon alternatives. One potential approach is the utilization of diverse forms of renewable energy, including solar radiation, wind power, and water flow. While established energy-harvesting infrastructures such as solar or wind farms, as well as hydroelectric dams, are typically centralized, there is a growing need for distributed energy-harvesting facilities that can tap into dispersed energy sources found in nature.[1] This requirement is particularly significant in remote areas with limited access to centralized facilities. Among the various categories of energy, water holds substantial amounts of energy in multiple forms, such as water droplets,[2–4] tides and waves,[5] and phase changes.[6]

In daily life, water droplets, particularly rain droplets, serve as an untapped mechanical energy source with significant abundance and universality. The exploration of energy harvesting from water droplets dates back as early as 1867.[7] Recently, various devices have been proposed to capture the potential and electrostatic energy of water droplets, such as piezoelectric[8] and triboelectric nanogenerators.[2–4] Among these, droplet generators (DGs), a type of triboelectric nanogenerator that relies on the interaction between water droplets and triboelectric materials, have witnessed rapid development.[7,9–14] For example, in pioneering research on droplet energy generation,[2] the generated voltage from a single droplet was approximately 9.3 V. By incorporating an additional top electrode, facilitating charge transfer between electrodes, the output voltage was enhanced to 143.5 V.[3] Subsequent advancements in surface treatment techniques enabled the generation of even higher voltages, reaching 225 V for high-frequency water droplets.[4] However, apart from the pursuit of higher voltages, several practical considerations need to be addressed. For instance, solution-based materials[2,3] tend to be costly for large-scale applications. Besides, some associated material processing imposes extra technical and sustainability barriers: e.g., reactive ion etching requires precise parameter control within vacuum chambers. Additionally, the employment of greenhouse gases such as sulfur hexafluoride raises concerns due to its detrimental impact on the environment.[4]

In this work, we present an economical fabrication method using readily available materials with no need for cleanroom settings. By utilizing solid polytetrafluoroethylene (PTFE) films with a thickness of approximately 10 mil, we were able to decrease the capacitance of a

[1]Material Science Engineering, Physical Science Engineering Division, King Abdullah University of Science and Technology, Thuwal 23955-6900, Saudi Arabia
[2]Shared Instrumentation Laboratories, School of Engineering & Applied Sciences, The State University of New York at Buffalo, Buffalo, NY 14260, USA
[3]Department of Electrical Engineering, The State University of New York at Buffalo, Buffalo, NY 14260, USA
[4]Applied Physics, Physical Science Engineering Division, King Abdullah University of Science and Technology, Thuwal 23955-6900, Saudi Arabia
[5]Mechanical Engineering, Physical Science Engineering Division, King Abdullah University of Science and Technology, Thuwal 23955-6900, Saudi Arabia
[6]Water Desalination and Reuse Center, Division of Biological Sciences and Engineering, King Abdullah University of Science and Technology, Thuwal 23955-6900, Saudi Arabia
[7]These authors contributed equally
[8]Lead contact
*Correspondence: qiaoqiang.gan@kaust.edu.sa
https://doi.org/10.1016/j.isci.2024.109291

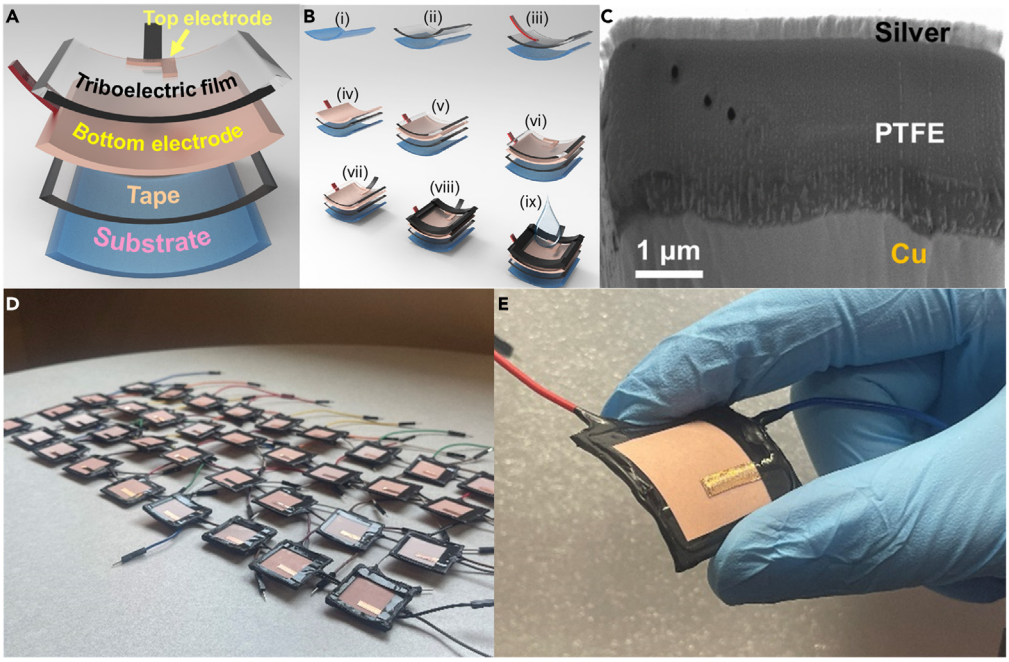

Figure 1. Inexpensive large-scale manufacture procedure

(A) Schematic of a typical device.

(B) Fabrication process of a DG. (i) A polypropylene substrate (blue). (ii) A 3M double-sided tape (light gray) on the substrate. (iii) Adhere an electric wire (red) on the double-sided tape. (iv) Place a copper (Cu) tape (pink) on top with the metal side facing down and the adhesive side facing up. (v) Place a PTFE film (transparent) on top. (vi) Place an L-shaped Cu tape (pink) as the top electrode. (vii) Adhere an electric wire (dark gray) by a second Cu tape (pink). (viii) Seal the four edges with an electrical tape (black). (ix) Drop cast Teflon solution on top of a device.

(C) SEM image of the air-dried 200-μL Teflon layer.

(D) Photograph of 36 devices.

(E) Photograph showing the flexibility of a DG.

droplet-induced electricity generator. As a result, we achieved a significant enhancement in the open circuit voltage (V_{oc}), reaching approximately 282.2 ± 27.9 V. This value exceeded the previously reported records by approximately 60 V (i.e., 225 V reported by ref.[4]). The remarkable aspect of our approach is that the entire device can be manually constructed, without the need for complex or expensive physical,[15–17] chemical,[18–20] or biological[21,22] modifications of the PTFE films.[23] Importantly, to achieve the optimized thickness, the estimated cost of solid PTFE films can be reduced by four orders of magnitude, comparing with that of the solution-based materials used in earlier pioneering devices.[3] Furthermore, we conducted a comprehensive investigation into two factors that influence the V_{oc} when increasing the thickness of the PTFE films: (1) the decrease in capacitance, and (2) the reduction in electrostatically induced charges. This investigation unveiled a notable tradeoff between the thickness of PTFE films and V_{oc}. To further showcase the practical application of DG, we scrutinized the criteria to harmonize DGs and light-emitting diodes (LEDs). The targets were to power more LEDs and produce uniform light patterns, aspects that were largely unexplored previously. We ascertained that relatively small turn-on voltages and similar current-voltage characteristics were essential. Leveraging the cost-effective triboelectric materials and LEDs with reasonably uniform characteristics, we achieved the successful powering of 100 LEDs simultaneously using a single device. Moreover, by employing an array of these economical devices, we demonstrated the creation of diverse light patterns, ensuring substantially uniform light intensity across each LED, and showcasing their potential for practical energy harvesting applications.

RESULTS

The schematic representation of a typical DG (e.g.,[3,4,24,25]) is shown in Figure 1A: A triboelectric film is sandwiched between a top and a bottom electrode. The objective of this study is to enhance V_{oc} by tuning the triboelectric film. Given the relationship between V_{oc}, capacitance (C), and charge (Q), i.e., $V_{oc} = Q/C$, a feasible method to achieve higher V_{oc} is to decrease C. The value of this C can be readily reduced by employing thicker triboelectric films, which is the general design principle. For instance, a linear positive correlation was reported between peak V_{oc} and the thickness of the PTFE film.[3] However, the comprehensive exploration of this phenomenon has been hindered by cost constraints: i.e., the solution-based materials used in earlier reports[2,3] are prohibitively expensive (e.g., AF 1601 × 6% solution used in ref.[3], which retails at $1,945/100 mL[26]). Employing this solution, along with drop-casting and curing processes, to create thicker PTFE films would inevitably escalate raw material expenses associated with validating the general design principle. Meanwhile, this type of DGs demand large

scales for effective mechanical energy harvesting from droplets (for instance, from rain droplets), necessitating the development of cost-effective devices utilizing simpler procedures and more affordable materials.

To achieve cost-effective production on a large scale, we have developed a simple method for constructing DGs using commercially available films, as depicted in Figure 1B. The process begins with a flexible square polypropylene (PP) sheet, measuring 3 cm × 3 cm in area and approximately 250 μm in thickness, serving as the substrate (Figure 1Bi). This substrate is then covered with a double-sided tape (Figure 1Bii), to firmly secure the bottom terminal (Figure 1Biii). The construction continues by sequentially applying a copper (Cu) conductive tape (Figure 1Biv) and a commercially available solid PTFE film (ePlastics, Figure 1Bv). The Cu tape acts as the bottom electrode, while the PTFE film serves as the functional triboelectric layer. Additionally, a small L-shaped Cu conductive tape is positioned on top of the PTFE film (Figure 1Bvi) and connected to the top terminal (Figure 1Bvii) to serve as the top electrode. To protect the device's contacts, all edges are sealed with electrical tape (Figure 1Bviii, 3M electrical insulating black polyester film with high solvent resistance). Next, the entire device undergoes compression using a laminator at 50°C to enhance contact between adjacent layers. In the final step illustrated in Figure 1Bix, a uniform 200-μL Teflon solution is drop-cast onto the top surface and air-dried for 8 h. This process further strengthens the contact between the PTFE film and the top electrode. To determine the thickness of this air-dried Teflon layer, we conducted scanning electron microscopy (SEM) characterization. For improved image contrast in the SEM profile, another Teflon layer was fabricated using the same method and sandwiched between a highly conductive Cu electrode and silver layer rather than within the device. Notably, the solution-based Teflon layer has a thickness of approximately 2.8 μm (Figure 1C), significantly thinner than the commercially available solid PTFE films used in Figure 1Bv (more technical details are listed in STAR Methods). Thus, the cost-effective utilization of these inexpensive films eliminates the need for costly solution-based materials mentioned in ref.[3] while satisfying the requirement for a thick PTFE film as per the general design principle.

Importantly, the thickness of the solid PTFE films can be conveniently adjusted over a wide range, extending to hundreds of micrometers. This flexibility allows for the cost-effective exploration of the device's thickness-dependent characteristics. Furthermore, the entire construction process can be carried out without the need for specialized laboratory facilities, enabling the potential for the mass production of affordable devices using industrial processes. A photograph in Figure 1D showcases 36 devices fabricated at a total cost of approximately $150 (detailed cost analysis available in STAR Methods). All materials employed in this manufacturing process are flexible and bendable, as demonstrated in Figure 1E, facilitating the integration of the fabricated devices with various substrates of different shapes. With the construction process outlined, next, we proceed to characterize the performance of this easily fabricated and cost-effective DG device.

DISCUSSION

As demonstrated in Figure 2A, when a tap-water droplet (with a volume of approximately 145 μL and a conductivity of about 288.6 μS/cm) impacts the device, an electric double layer (EDL) was established at the liquid-solid interface. When the droplet slides down, the EDL is disrupted, breaking the electric neutrality at the interface.[27] Therefore, charges are introduced due to liquid-solid contact electrification[3] and subsequently stored within the PTFE film. Concurrently, charges are also induced in the electrodes via electrostatic induction,[3,25] as depicted in the cross-sectional structure in Figure 2B. Upon spreading and contact of the droplet with the top Cu electrode, a closed circuit forms (Figure 2C), facilitating charge transfer between the two electrodes. Consequently, a voltage pulse is excited until the droplet disengages from the top Cu electrode. The controlled smooth movement of water droplets and their departure from the PTFE film are ensured by the hydrophobic PTFE film (with a contact angle, θ, of 91.2°, as demonstrated in Figure 2D). The circuit then reverts to the open state in Figure 2A. This voltage pulse can be characterized using an oscilloscope connected with the electrical wires (Figure 2E). As a result, the measured time-dependent V_{oc} of a DG made by a 10-mil-thick PTFE film (~254 μm) is depicted in Figure 2F. Notably, this device generates an averaged peak V_{oc} of 282.2 ± 27.9 V, which is approximately twice that reported in the pioneering work[3] (approximately 143.5 V), and exceeded the previously reported records by approximately 60 V.[4] As shown in Figure 2G, the width of a typical voltage pulse (i.e., the pulse indicated by the arrow in Figure 2F) was around 29 ms (i.e., spanning from 7.623 s to 7.652 s, when the pulse value returns to 0 as indicated by the red color in Figure 2G. See other pulse widths in STAR Methods; Figure S1 in the supplemental information).

This enhanced averaged peak V_{oc} demonstrates that solid PTFE films are promising in meeting the demand for thick PTFE films as prescribed by the general design principle, yet at a substantially reduced cost compared with solution-based materials.[3] For instance, a 9-cm^2 solid PTFE film costs between $0.028 and $0.113 (corresponding to thicknesses ranging from 5 to 20 mils), a cost that could be further reduced through mass production.[28] Consequently, our proposed device shows potential to overcome the cost barrier to manufacturing large-scale DG devices. However, when using a PTFE film with a thickness of approximately 10 mils in a DG device, the resulting V_{oc} is only about twice that of devices incorporating solution-based PTFE films mentioned in ref.[3], which have thicknesses one or two orders of magnitude thinner.

To further investigate the influence of thicker PTFE films in our devices, we utilized a variety of commercially available PTFE films with thicknesses spanning from approximately 127 μm–508 μm (corresponding to ~5 mil, ~10 mil, ~15 mil, and ~20 mil, respectively). For each thickness, three devices were constructed and their characteristics are represented in Figure 2H (denoted by black spheres). The averaged peak V_{oc} reached its maximum at 282.2 ± 27.9 V when the PTFE film was ~10 mil, and displayed a decreasing trend with thicker PTFE films, once again contradicting the general design principle. These unexpected results suggest that a higher V_{oc} production is not solely dependent on the smaller capacitance. Other factors may also determine the device performance, as will be explored later in discussion.

To reveal why thicker solid PTFE films possibly yield lower rather than higher V_{oc}, it is crucial to better understand the role these films play in DGs. In particular, it is necessary to characterize the transferred charge (Q) between the two Cu electrodes using a nanocoulomb meter (i.e., refer to STAR Methods and see the photograph of the setup in Figure S2 in the supplemental information). As depicted in Figure 2I, the peak Q for a device with a 5-mil-thick PTFE film was approximately 29.5 nC. Notably, this peak Q is smaller than that generated by the

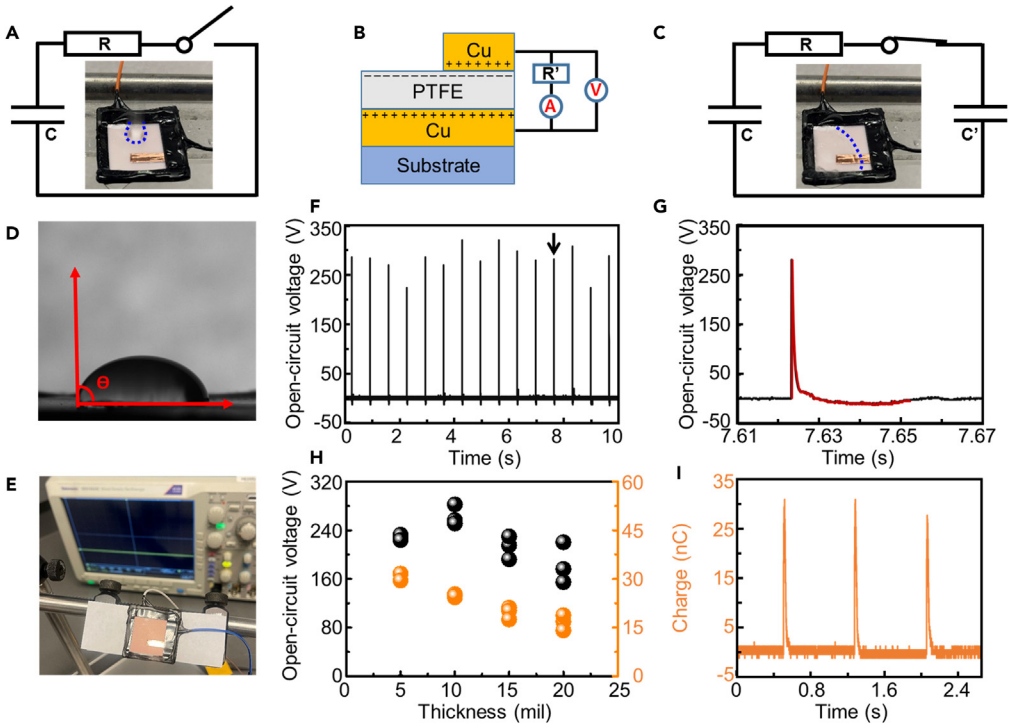

Figure 2. Device characterization

The (A) open and (C) closed circuit models (A) before and (C) after the water droplet connected the PTFE and the top Cu electrode, respectively. The edges of the water droplets are highlighted by the blue dashed curves to guide the eye. In the circuits, R is the impedance of the water droplet and the external load, C is the total capacitance of the PTFE plus the capacitor formed at the water/PTFE interface, and C′ is the capacitance of the capacitor formed at the water/top Cu interface.

(B) The cross-sectional structure of a DG coupled with a circuit to characterize the electrical performance.

(D) The contact angle of a droplet on the device.

(E) Photograph of the characterization setup for the measurement of the open-circuit voltage (V_{oc}).

(F) The time-dependent V_{oc} values in 10 s.

(G) The V_{oc} pulse indicated by the black arrow in (F).

(H) The averaged peak V_{oc} and the averaged peak transferred charge (Q) measured from DGs with various PTFE thicknesses.

(I) The time-dependent Q between the two Cu electrodes for a DG with a 5-mil-thick PTFE film.

solution-based materials (e.g., 49.8 nC[3]). Consequently, it is this smaller peak Q that restricts the DG with solid PTFE films from generating the high V_{oc} anticipated by the general design principle.

The peak Q for the remaining devices was also characterized and shown in Figure 2H (represented by orange spheres). When the thickness escalated from 5 mil to 20 mil, the averaged peak Q predominantly displayed a declining trend. This decrease in peak Q can be ascribed to the larger induction distance needed to electrostatically induce charges in the electrodes.[29,30] According to the Coulomb's law, the magnitude of the electric field of a point charge, E, is inversely proportional to the square of the distance from the point charge, r, i.e., $E = kq/r^2$. Here, k is Coulomb's constant, and q is the magnitude of the point charge, which corresponds to the charges originating from liquid-solid contact electrification on the top surface of the PTFE film. An increased thickness of the PTFE film implies a greater distance between its top surface and the bottom Cu electrode (Figure 2B). This greater distance led to a weaker electric field and fewer electrostatically induced charges in the bottom Cu electrode. Ultimately, the transferred charge (Q) between the two Cu electrodes declined with an increasing thickness of the PTFE films (Figure 2H). Therefore, while the general design principle predicts that thicker PTFE films would yield higher V_{oc}, the reduced averaged peak Q, resulting from Coulomb's law, indicates that the thickness of the PTFE film cannot be increased indefinitely. This practical limitation was not revealed in the pioneering work.[3] It is important to note that despite alterations in the charge distribution, the water droplets can still successfully complete the open circuit, a prerequisite for voltage generation (see the molecular dynamics simulations in STAR Methods and Figure S3 in the supplemental information). After characterizing the electrical performance of the devices, our next objective is to demonstrate its practical application.

Droplets are a ubiquitous occurrence in our daily lives, originating from various sources such as river runoff, rainfall, natural condensation on surfaces such as leaves and windows, micro-droplets within irrigation systems, and even water pipe leaks. The widespread availability of these droplets positions cost-effective DGs as an innovative power source, enabling the operation of energy-efficient devices, including sensors and LEDs. Previous studies largely investigated how the performance of the DGs can be affected by the properties of droplets, such as

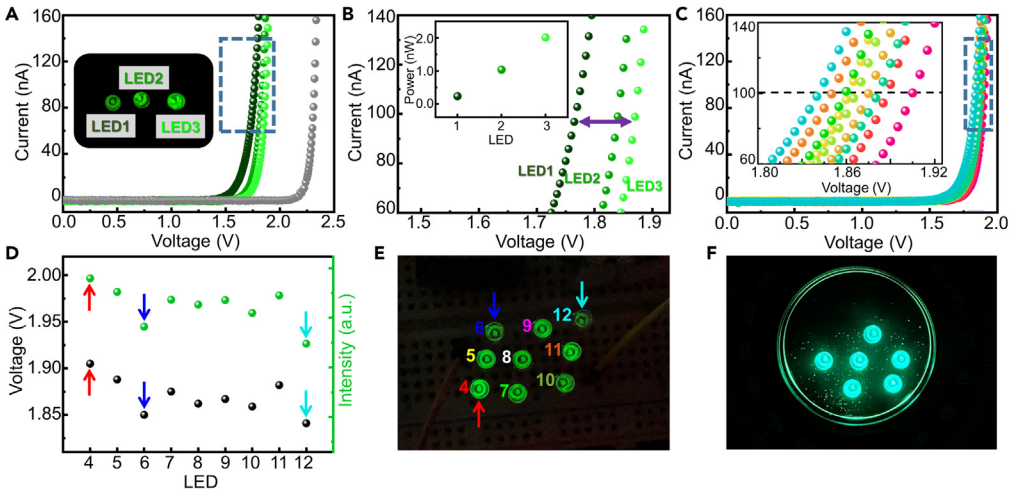

Figure 3. DG and LED pairing

(A) The current-voltage characteristics of three green LEDs (green dots) and one white LED (gray dots), respectively. Inset: Photograph of the three green LEDs in series.

(B) The zoomed-in current-voltage characteristics of the three green LEDs near 100 nA. Inset: Emitted power at 530 nm of the three LEDs measured by a silicon detector.

(C) The current-voltage characteristics of the nine green LEDs. Inset: The zoomed-in current-voltage characteristics near 100 nA.

(D) The voltages (black) and the light intensities (green) of the nine green LEDs at 100 nA.

(E) Photograph of the nine green LEDs in series.

(F) Photograph of the remaining six green LEDs in series after removing the three most discrepant LEDs.

temperature,[31] salt concentration[3,24,32–34] and pH.[24] Additionally, while previous studies have demonstrated the feasibility of powering LEDs using DGs,[3] the factors governing the selection of compatible DG and LED pairs remain ambiguous. Neglecting the inherent compatibility between DGs and LEDs may lead to confusion among operators when some LEDs fail to illuminate successfully driven by given DGs or as brightly as those reported in pioneering research.[3] In this context, we delve into this critical aspect, elucidating the essential criteria necessary for the practical realization of future DG-based LED systems.

The peak output intensity of semiconductor LEDs can be modulated using pulsed voltage or current,[35] typically in the form of square or rectangular waves, through the application of pulse width modulation techniques. However, it is noteworthy that these square or rectangular pulsed voltages are significantly different from those generated by the DGs shown in Figure 2F. In particular, the LED may not be lighted if its intrinsic property is not well matched with the DG output. Therefore, two additional aspects warrant consideration in practical applications to achieve bright output from LEDs.

Firstly, to maximize the number of LEDs powered by a given DG, it is crucial to minimize the LEDs' turn-on voltage. While this principle is straightforward, choosing LED products in the market with lower turn-on voltages can be less apparent. The turn-on voltage of an LED is primarily determined by the bandgap of its emissive material. Consequently, LEDs emitting longer wavelength light (e.g., IR LEDs) typically exhibit lower turn-on voltages. To further reduce the turn-on voltage, the concept of bias-perturbed carriers located at the non-thermal-equilibrium band edge in various LED types were reported (for III-V semiconductors, quantum dots, organics, and perovskite LEDs),[36] known as "thermophotonic cooling" or "electroluminescent cooling."[37] For example, InGaAsP-based IR LEDs have demonstrated an ultra-low turn-on voltage of 0.54 V.[36] Additionally, strategies such as reducing series resistance (comprising bulk resistance and contact resistance[36]) and enhancing external quantum efficiency (e.g., designing quantum wells and high-quality interfaces[38]) can further decrease the turn-on voltage. To facilitate LED selection for other researchers, we have provided a comprehensive list of turn-on voltages for various LEDs in STAR Methods and Table S1 in the supplemental information. In this study, we opted for visible LEDs to allow for the straightforward visual assessment of the DGs' capabilities. In Figure 3A, we measured the current-voltage characteristics of four commercially available LEDs: three green LEDs (model zc-323GC-4) and one white LED (model zc-323WC-4 from Beijing 9e Laser Technology Ltd.). As depicted by the green dots, the green LEDs exhibited a turn-on voltage of approximately 1.6 V. In contrast, the gray dots indicate a turn-on voltage of approximately 2.1 V for the white LED, notably higher than that of the green LEDs. Therefore, to power a greater number of LEDs with a given DG, LEDs with lower turn-on voltages (i.e., green LEDs in our experiment) are desired.

Secondly, to achieve uniform light patterns, it is vital to refrain from integrating LEDs with varying current-voltage characteristics when connecting multiple LEDs in series within a circuit. Figure 3B presents a zoomed-in image of the blue dashed rectangle in Figure 3A, detailing the current-voltage characteristics of the three green LEDs (i.e., LED1, LED2, and LED3) at a current of approximately 100 nA. When arranged in a series configuration, these LEDs are anticipated to carry the same current. However, despite this identical current, slight discrepancies in voltage drops emerged, as indicated by the violet arrow in Figure 3B. Among these three samples, the voltage drop across LED3 was the

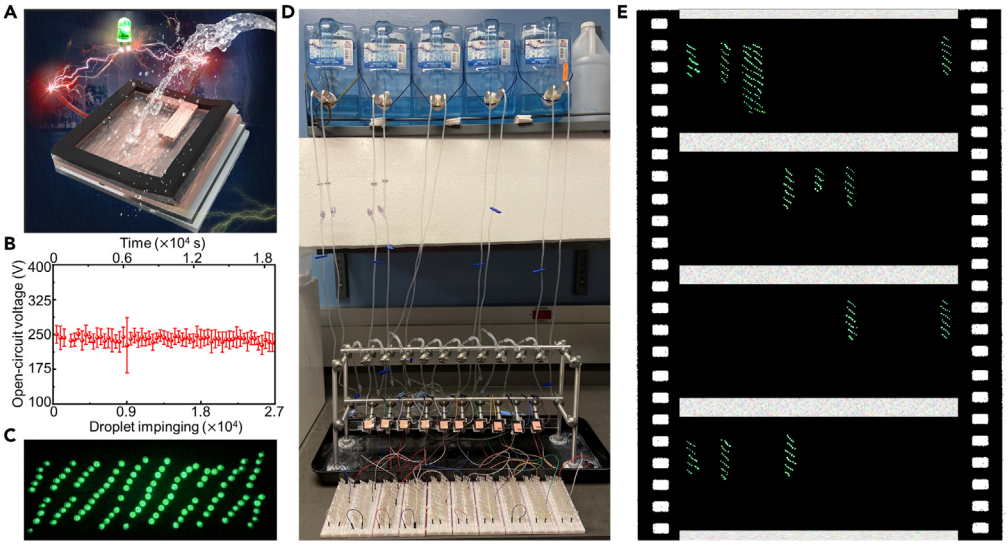

Figure 4. Application demo of DGs

(A) Schematic of a DG powering an LED.

(B) The averaged peak V_{oc} with increasing droplet impinging times. The error bars correspond to the standard deviation of the measurements.

(C) Photograph of 100 LEDs powered by a DG.

(D) An array of ten DGs to power different numbers of LEDs.

(E) Video frames of an operational array of LEDs powered by the DG array at different moments, showing different light patterns.

largest (light green dots, ~1.87 V), while that across LED1 was the smallest (dark green dots, ~1.77 V). As a result, LED3, consuming more power (note that the power consumed by an LED is given by V×I passing through the device), emitted a brighter light than LED1 and LED2, as visually demonstrated by the photograph in the inset of Figure 3A. It is worth noting that commercial LED packages emit directional light due to the epoxy-encapsulated LED package with a parabolic lens. Therefore, it is necessary to align LEDs toward the same direction during this test (see technical details in STAR Methods and Figure S4 in the supplemental information). One can see from the inset of Figure 3B, the output power at 530 nm was subsequently measured using a silicon detector, confirming that LED3 was the brightest. Therefore, to obtain a uniform light pattern, the uniformity of the LEDs is imperative.

Following these criteria, we conducted an in-depth analysis of nine green LEDs (specifically, LED4 to LED12) sourced from the same batch, with a particular focus on assessing their uniformity. The current-voltage characteristics displayed in Figure 3C reveal distinct variations among these LEDs, particularly highlighted in the zoomed-in section near a current of approximately 100 nA (inset). It is evident that the voltage levels for these nine LEDs ranged from 1.84 to 1.91 V, with a coefficient of variation (CV) of 1.00% (i.e., standard deviation/average, as depicted by the black dots in Figure 3D). Consequently, the nonuniformity in the light emitted by these LEDs was discernible to the naked eye, as illustrated in the photograph in Figure 3E: two LEDs appeared visibly dimmer (LED6 and LED12, indicated by blue and cyan arrows, respectively), while one shone noticeably brighter than the others (LED4, highlighted by a red arrow).

For a more rigorous quantitative analysis, we analyzed the light intensity emitted by each LED (represented by the green dots in Figure 3D, with detailed information available in STAR Methods; Figure S5; Table S2 in the supplemental information). This analysis unveiled a significant deviation in emitted light intensity, amounting to 18.29%. Clearly, Figure 3D underscores a strong correlation between the voltage fluctuation pattern and the variations in light intensity. This type of nonuniformity had also been observed in earlier pioneering works[3,4] (refer to STAR Methods and Figure S6 in the supplemental information), potentially stemming from fluctuations in the LED characteristics. To address this issue, we systematically removed the three most discrepant LEDs from the circuit (namely, LED4, LED6, and LED12). As a result, the applied voltage redistributed across the remaining six LEDs, which possessed more consistent features. In contrast to the scenario depicted in Figures 3E and 3F demonstrates a notably uniform light intensity across all LEDs. Remarkably, the CV values for both voltage and light intensity were substantially reduced to 0.67% and 3.10%, respectively (see additional details in STAR Methods, Figure S7; Table S3 in the supplemental information). The pursuit of an even higher level of uniformity could be considered by removing more discrepant LEDs, with a cautious approach to prevent the breakdown of the remaining LEDs. This unequivocally affirms the effectiveness of our refined LED selection criteria in achieving compatibility with the DG devices by using LEDs with low turn-on voltages and uniform current-voltage characteristics.

Using LEDs with reasonably uniform characteristics (see STAR Methods and Figure S8 for more details in the supplemental information), we proceeded to demonstrate the droplet-powered lighting application employing our optimized DG devices (Figure 4A). The durability and stability were first investigated by continuous measurements of the time-dependent V_{oc}. Over 2.7×10^4 droplets were impinged on the device at an approximate rate of ~0.7 s per droplet (i.e., approximately 5.25 h). Figure 4B presents the averaged peak V_{oc} as the times increased. Each data point represents the average peak V_{oc} values collected within a 10-s interval. Only a slight decrease occurred in the averaged peak

V_{oc}, attesting to the robustness of our devices, which is important in practice. Next, we performed a droplet-powered lighting experiment using DGs with the functional layer of a 10-mil-thick solid PTFE film. When a single droplet was released from a height of ~15 cm, it could instantaneously power 100 commercial green LEDs (see Figure 4C and Video S1 in the supplemental information). The resulting light intensities across the LEDs was notably uniform compared with ref.[4] (see Figure S6B in the supplemental information). To reveal the scalability of our cost-effective devices, an array of ten DGs were employed to light up the LEDs (Figure 4D). By connecting different numbers of LEDs into the load circuit, our devices demonstrated the potential to produce diverse light patterns when the droplet release frequency for each device slightly varied (see Figure 4E for photographs at different moments and Video S2 in the supplemental information). The controllability of the light patterns can be further improved by integrating additional flow switches for the water droplets (e.g., programmable switches used in droplet displays[39]).

In conclusion, we have successfully engineered droplet-induced electricity generators that leverage off-the-shelf solid PTFE films and tapes. The manufacturing process stands out for its simplicity, cost-effectiveness, and scalability, all achieved without the need for intricate or expensive cleanroom facilities. These advantages and benefits enable us to delve into the effect of the PTFE thickness on V_{oc}, a subject insufficiently tackled in previous studies.[2,3] While the general design principle suggests that increased PTFE film thickness and thus decreased capacitance should yield a higher V_{oc}, there exists a practical boundary imposed by Coulomb's law, leading to the decline in electrostatically induced charges. Our efforts culminated in an impressive average peak V_{oc} of approximately 282.2 $\pm$ 27.9 V at an optimized thickness of approximately 10 mil. Our refined DG device can power 100 LEDs simultaneously, demonstrating its robust performance. Moreover, the arrangement of these optimized devices showcased their ability to generate diverse light patterns instantaneously using LEDs. This underscores their potential for large-scale energy harvesting applications. In implementing DGs as power sources, we clarified the requirements for LEDs, ensuring alignment with the distinctive pulsed voltage characteristics generated by DGs. Intriguingly, this technology unveils the possibility of driving LEDs or low-power sensors in dim environments without relying on grid electricity. For instance, envision the creation of LED signals during nights or early mornings when natural condensation occurs. Additionally, the concept extends to constructing an Internet of Things network in obscured spaces where complex water pipes are situated, indicating the versatility and far-reaching impact of inexpensive and durable DGs.

Limitations of the study

We regret that we currently lack the facilities necessary to measure the current of the device, which, in turn, prevented us from calculating the generated power and the energy conversion efficiency. While we acknowledge the importance of these metrics, we believe that the practical application demonstration, e.g., powering 100 LEDs concurrently, serves as a tangible illustration of the device's generated power. Besides, we acknowledge the importance of demonstrating extended durability for practical applications. The primary factor influencing the durability of our device is the contact between the PTFE films and the top Cu electrodes. We will explore ways to provide a more thorough assessment of the device's durability in future work.

STAR★METHODS

Detailed methods are provided in the online version of this paper and include the following:

- KEY RESOURCES TABLE
- RESOURCE AVAILABILITY
  - Lead contact
  - Materials availability
  - Data and code availability
- METHOD DETAILS
  - Device fabrication and measurement
  - Cost estimation of the materials in a thin-film droplet-induced electricity generator
  - The pulse widths of voltage pulses
  - The photograph of the setup to measure the transferred charge
  - Molecular dynamics simulations
  - LEDs with small turn-on voltages
  - The spatial distribution and the optical setup for LEDs
  - The voltages and light intensities of the nine LEDs
  - The uniformity of LEDs in previous demonstrations
  - The voltages and light intensities of the remaining six LEDs
  - The current-voltage characteristics of ten LEDs

SUPPLEMENTAL INFORMATION

Supplemental information can be found online at https://doi.org/10.1016/j.isci.2024.109291.

ACKNOWLEDGMENTS

H.S. and Z.B. contributed equally to this work. The authors appreciate Dr. Wenhong Yang for the support of the visualization of Figures 1A, 1B and, 4A. This work was supported by a baseline from the King Abdullah University of Science and Technology (BAS/1/1415-01).

AUTHOR CONTRIBUTIONS

H.S.: conceptualization (supporting); data curation (lead); formal analysis (lead); methodology (equal); software (supporting); writing/original draft preparation (lead); and writing /review and editing (equal). **Z.B.**: conceptualization (supporting) and data curation (supporting). **A.S.V. and U.S.**: software (supporting); formal analysis (lead); writing /review and editing (supporting). **U.P.U.K.**: data curation (supporting); formal analysis (supporting); software (lead); visualization (supporting); and writing /review and editing (supporting). **T.T.T**: writing/review and editing (supporting). **J.S.V.**: writing/review and editing (supporting). **Q.G.**: conceptualization (lead); funding acquisition (lead); methodology (equal); project administration (lead); writing /review and editing (equal).

DECLARATION OF INTERESTS

The authors declare no competing interests.

DECLARATION OF GENERATIVE AI AND AI-ASSISTED TECHNOLOGIES IN THE WRITING PROCESS

During the preparation of this work the authors used ChatGPT in order to improve language. After using this tool/service, the authors reviewed and edited the content as needed and take full responsibility for the content of the publication.

Received: December 5, 2023
Revised: February 8, 2024
Accepted: February 16, 2024
Published: February 21, 2024

REFERENCES

1. Mitchell, C. (2016). Momentum is increasing towards a flexible electricity system based on renewables. Nat. Energy *1*, 15030. https://doi.org/10.1038/Nenergy.2015.30.
2. Lin, Z.H., Cheng, G., Lee, S., Pradel, K.C., and Wang, Z.L. (2014). Harvesting water drop energy by a sequential contact-electrification and electrostatic-induction process. Adv. Mater. *26*, 4690–4696. https://doi.org/10.1002/adma.201400373.
3. Xu, W., Zheng, H., Liu, Y., Zhou, X., Zhang, C., Song, Y., Deng, X., Leung, M., Yang, Z., Xu, R.X., et al. (2020). A droplet-based electricity generator with high instantaneous power density. Nature *578*, 392–396. https://doi.org/10.1038/s41586-020-1985-6.
4. Wang, L., Song, Y., Xu, W., Li, W., Jin, Y., Gao, S., Yang, S., Wu, C., Wang, S., and Wang, Z. (2021). Harvesting energy from high-frequency impinging water droplets by a droplet-based electricity generator. EcoMat *3*, e12116. https://doi.org/10.1002/eom2.12116.
5. Wang, Z.L., Jiang, T., and Xu, L. (2017). Toward the blue energy dream by triboelectric nanogenerator networks. Nano Energy *39*, 9–23. https://doi.org/10.1016/j.nanoen.2017.06.035.
6. Chen, X., Goodnight, D., Gao, Z., Cavusoglu, A.H., Sabharwal, N., DeLay, M., Driks, A., and Sahin, O. (2015). Scaling up nanoscale water-driven energy conversion into evaporation-driven engines and generators. Nat. Commun. *6*, 7346. https://doi.org/10.1038/ncomms8346.
7. Dong, J., Fan, F.R., and Tian, Z.Q. (2021). Droplet-based nanogenerators for energy harvesting and self-powered sensing. Nanoscale *13*, 17290–17309. https://doi.org/10.1039/d1nr05386h.
8. Guigon, R., Chaillout, J.J., Jager, T., and Despesse, G. (2008). Harvesting raindrop energy: experimental study. Smart Mater. Struct. *17*, 015039. https://doi.org/10.1088/0964-1726/17/01/015039.
9. Wang, Z.L., and Wang, A.C. (2019). On the origin of contact-electrification. Mater. Today *30*, 34–51. https://doi.org/10.1016/j.mattod.2019.05.016.
10. Xu, W., and Wang, Z. (2020). Fusion of slippery interfaces and transistor-inspired architecture for water kinetic energy harvesting. Joule *4*, 2527–2531. https://doi.org/10.1016/j.joule.2020.09.007.
11. Kim, D.W., Lee, J.H., Kim, J.K., and Jeong, U. (2020). Material aspects of triboelectric energy generation and sensors. NPG Asia Mater. *12*, 6. https://doi.org/10.1038/s41427-019-0176-0.
12. Yu, Y., Li, H., Zhao, D., Gao, Q., Li, X., Wang, J., Wang, Z.L., and Cheng, T. (2023). Material's selection rules for high performance triboelectric nanogenerators. Mater. Today *64*, 61–71.
13. Chen, A., Zhang, C., Zhu, G., and Wang, Z.L. (2020). Polymer materials for high-performance triboelectric nanogenerators. Adv. Sci. *7*, 2000186. https://doi.org/10.1002/advs.202000186.
14. Cheng, T., Shao, J., and Wang, Z.L. (2023). Triboelectric nanogenerators. Nat. Rev. Methods Primers *3*, 39.
15. Lee, K.Y., Chun, J., Lee, J.H., Kim, K.N., Kang, N.R., Kim, J.Y., Kim, M.H., Shin, K.S., Gupta, M.K., Baik, J.M., and Kim, S.W. (2014). Hydrophobic sponge structure-based triboelectric nanogenerator. Adv. Mater. *26*, 5037–5042. https://doi.org/10.1002/adma.201401184.
16. Chen, J., Zhu, G., Yang, W., Jing, Q., Bai, P., Yang, Y., Hou, T.C., and Wang, Z.L. (2013). Harmonic-resonator-based triboelectric nanogenerator as a sustainable power source and a self-powered active vibration sensor. Adv. Mater. *25*, 6094–6099. https://doi.org/10.1002/adma.201302397.
17. Yu, Y., Li, Z., Wang, Y., Gong, S., and Wang, X. (2015). Sequential infiltration synthesis of doped polymer films with tunable electrical properties for efficient triboelectric nanogenerator development. Adv. Mater. *27*, 4938–4944. https://doi.org/10.1002/adma.201502546.
18. Li, S., Fan, Y., Chen, H., Nie, J., Liang, Y., Tao, X., Zhang, J., Chen, X., Fu, E., and Wang, Z.L. (2020). Manipulating the triboelectric surface charge density of polymers by low-energy helium ion irradiation/implantation. Energy Environ. Sci. *13*, 896–907. https://doi.org/10.1039/c9ee03307f.
19. Lee, J.W., Jung, S., Lee, T.W., Jo, J., Chae, H.Y., Choi, K., Kim, J.J., Lee, J.H., Yang, C., and Baik, J.M. (2019). High-output triboelectric nanogenerator based on dual inductive and resonance effects-controlled highly transparent polyimide for self-powered sensor network systems. Adv. Energy Mater. *9*, 1901987. https://doi.org/10.1002/aenm.201901987.
20. Wang, S., Xie, Y., Niu, S., Lin, L., Liu, C., Zhou, Y.S., and Wang, Z.L. (2014). Maximum surface charge density for triboelectric nanogenerators achieved by ionized-air injection: methodology and theoretical understanding. Adv. Mater. *26*, 6720–6728. https://doi.org/10.1002/adma.201402491.
21. Zhang, Y., Zhou, Z., Sun, L., Liu, Z., Xia, X., and Tao, T.H. (2018). "Genetically engineered" biofunctional triboelectric nanogenerators using recombinant spider silk. Adv. Mater. *30*, e1805722. https://doi.org/10.1002/adma.201805722.

22. Wang, R., Gao, S., Yang, Z., Li, Y., Chen, W., Wu, B., and Wu, W. (2018). Engineered and laser-processed chitosan biopolymers for sustainable and biodegradable triboelectric power generation. Adv. Mater. *30*, 1706267. https://doi.org/10.1002/adma.201706267.
23. Zhou, Y., Deng, W., Xu, J., and Chen, J. (2020). Engineering materials at the nanoscale for triboelectric nanogenerators. Cell Rep. Phys. Sci. *1*, 100142. https://doi.org/10.1016/j.xcrp.2020.100142.
24. Wu, H., Mendel, N., van der Ham, S., Shui, L., Zhou, G., and Mugele, F. (2020). Charge trapping-based electricity generator (CTEG): An ultrarobust and high efficiency nanogenerator for energy harvesting from water droplets. Adv. Mater. *32*, e2001699. https://doi.org/10.1002/adma.202001699.
25. Wang, X., Fang, S., Tan, J., Hu, T., Chu, W., Yin, J., Zhou, J., and Guo, W. (2021). Dynamics for droplet-based electricity generators. Nano Energy *80*, 105558. https://doi.org/10.1016/j.nanoen.2020.105558.
26. https://pages.chemours.com/Teflon-Industrial—Amorphous-Fluoro_Amourphous-Fluoroplastic-Resins.html.
27. Wang, N., Liu, Y., Ye, E., Li, Z., and Wang, D. (2023). Contact electrification behaviors of solid–liquid interface: Regulation, mechanisms, and applications. Adv. Energy Sustain. Res. 4, 2200186.
28. https://www.eplastics.com/sheets/ptfe.
29. Li, X., Tao, J., Wang, X., Zhu, J., Pan, C., and Wang, Z.L. (2018). Networks of high performance triboelectric nanogenerators based on liquid-solid interface contact electrification for harvesting low-frequency blue energy. Adv. Energy Mater. *8*, 1800705. https://doi.org/10.1002/aenm.201800705.
30. Mi, H.Y., Jing, X., Meador, M.A.B., Guo, H., Turng, L.S., and Gong, S. (2018). Triboelectric nanogenerators made of porous polyamide nanofiber mats and polyimide aerogel film: Output optimization and performance in circuits. ACS Appl. Mater. Interfaces *10*, 30596–30606. https://doi.org/10.1021/acsami.8b08098.
31. Xu, W., Zhou, X., Hao, C., Zheng, H., Liu, Y., Yan, X., Yang, Z., Leung, M., Zeng, X.C., Xu, R.X., and Wang, Z. (2019). SLIPS-TENG: robust triboelectric nanogenerator with optical and charge transparency using a slippery interface. Natl. Sci. Rev. *6*, 540–550. https://doi.org/10.1093/nsr/nwz025.
32. Jeon, S.B., Seol, M.L., Kim, D., Park, S.J., and Choi, Y.K. (2016). Self-powered ion concentration sensor with triboelectricity from liquid-solid contact electrification. Adv. Electron. Mater. *2*, 1600006. https://doi.org/10.1002/aelm.201600006.
33. Sun, Y., Huang, X., and Soh, S. (2015). Using the gravitational energy of water to generate power by separation of charge at interfaces. Chem. Sci. *6*, 3347–3353. https://doi.org/10.1039/c5sc00473j.
34. Choi, D., Kim, D.W., Yoo, D., Cha, K.J., La, M., and Kim, D.S. (2017). Spontaneous occurrence of liquid-solid contact electrification in nature: Toward a robust triboelectric nanogenerator inspired by the natural lotus leaf. Nano Energy *36*, 250–259. https://doi.org/10.1016/j.nanoen.2017.04.026.
35. Pattison, P.M., Tsao, J.Y., Brainard, G.C., and Bugbee, B. (2018). LEDs for photons, physiology and food. Nature *563*, 493–500. https://doi.org/10.1038/s41586-018-0706-x.
36. Lian, Y., Lan, D., Xing, S., Guo, B., Ren, Z., Lai, R., Zou, C., Zhao, B., Friend, R.H., and Di, D. (2022). Ultralow-voltage operation of light-emitting diodes. Nat. Commun. *13*, 3845. https://doi.org/10.1038/s41467-022-31478-y.
37. Sadi, T., Radevici, I., and Oksanen, J. (2020). Thermophotonic cooling with light-emitting diodes. Nat. Photon. *14*, 205–214. https://doi.org/10.1038/s41566-020-0600-6.
38. Li, N., Han, K., Spratt, W., Bedell, S., Ott, J., Hopstaken, M., Libsch, F., Li, Q., and Sadana, D. (2019). Ultra-low-power sub-photon-voltage high-efficiency light-emitting diodes. Nat. Photon. *13*, 588–592. https://doi.org/10.1038/s41566-019-0463-x.
39. https://www.youtube.com/watch?v=_z7lAxEMF74.
40. https://www.amazon.com/dp/B01LZF1ZSZ/.
41. https://www.digikey.com/en/products/detail/3m-tc/2-5-9088/3339783.
42. https://www.amazon.com/dp/B089R75V18/.
43. Thompson, A.P., Aktulga, H.M., Berger, R., Bolintineanu, D.S., Brown, W.M., Crozier, P.S., in't Veld, P.J., Kohlmeyer, A., Moore, S.G., Nguyen, T.D., et al. (2022). LAMMPS - a flexible simulation tool for particle-based materials modeling at the atomic, meso, and continuum scales. Comput. Phys. Commun. *271*, 108171. https://doi.org/10.1016/j.cpc.2021.108171.
44. Evans, D.J., and Holian, B.L. (1985). The Nose-Hoover thermostat. J. Chem. Phys. *83*, 4069–4074. https://doi.org/10.1063/1.449071.
45. Abascal, J.L.F., Sanz, E., García Fernández, R., and Vega, C. (2005). A potential model for the study of ices and amorphous water: TIP4P/Ice. J. Chem. Phys. *122*, 234511. https://doi.org/10.1063/1.1931662.
46. Ryckaert, J.-P., Ciccotti, G., and Berendsen, H.J. (1977). Numerical integration of the cartesian equations of motion of a system with constraints: molecular dynamics of n-alkanes. J. Comput. Phys. *23*, 327–341.
47. Lennard-Jones, J.E. (1931). Proc. Phys. Soc. *43*, 461–482.
48. Koneshan, S., Rasaiah, J.C., Lynden-Bell, R.M., and Lee, S.H. (1998). Solvent structure, dynamics, and ion mobility in aqueous solutions at 25°C. J. Phys. Chem. B *102*, 4193–4204. https://doi.org/10.1021/jp980642x.
49. Nejakar, S.M., and Pruthvi, S. (2014). Wireless infrared remote controller for multiple home appliances. Int. J. Electr. Electron. Res. *2*, 25–35.
50. Patel, C.T., Mistry, V.J., Desai, L.S., and Meghrajani, Y.K. (2018). Multisensor-based Object Detection in Indoor Environment for Visually Impaired People (IEEE), pp. 1023–1026.
51. Abaya, W.F., Basa, J., Sy, M., Abad, A.C., and Dadios, E.P. (2014). Low Cost Smart Security Camera with Night Vision Capability Using Raspberry Pi and OpenCV (IEEE), pp. 1–6.

STAR★METHODS

KEY RESOURCES TABLE

REAGENT or RESOURCE	SOURCE	IDENTIFIER
Chemicals, peptides, and recombinant proteins		
Teflon solution (amorphous fluoroplastic 400S2-100-1)	DuPont	https://pages.chemours.com/Teflon-Industrial—Amorphous-Fluoro_Amourphous-Fluoroplastic-Resins.html?_ga=2.86727064.1617540938.1601101400-1716363531.1601101400
Software and algorithms		
MATLAB	MathWorks	https://www.mathworks.com
Molecular dynamics simulations	LAMMPS	https://www.lammps.org
Other		
Polytetrafluoroethylene (PTFE) films	ePlastics	https://www.eplastics.com/PTFENAT0-005X12
Copper (Cu) double-sided conductive tapes	AIYUNNI-25	https://www.amazon.com/dp/B08LL27SVX

RESOURCE AVAILABILITY

Lead contact

Further information and requests for resources and reagents should be directed to and will be fulfilled by the lead contact, Qiaoqiang Gan (qiaoqiang.gan@kaust.edu.sa).

Materials availability

This study did not generate new materials.

Data and code availability

- All data reported in this paper will be shared by the lead contact upon request.
- This paper does not report original code.
- Any additional information required to reanalyze the data reported in this paper is available from the lead contact upon request.

METHOD DETAILS

Device fabrication and measurement

The droplet-induced electricity generators were fabricated with as-purchased double-sided tapes (3M 2-5-9088 in Figure 1Bii), electric wires (Haitronic copper jumper wire in Figure 1Biii), copper (Cu) double-sided conductive tapes (AIYUNNI-25 in Figure 1Biv), polytetrafluoroethylene (PTFE) films (ePlastics in Figure 1Bv), electrical tapes (3M electrical insulating black polyester film with high solvent resistance in Figure 1Bviii), liquid electrical tapes (Gardner Bender LTB-400), and Teflon solution (DuPont amorphous fluoroplastic 400S2-100-1, Figure 1Bix). Liquid electrical tapes were employed to further seal the edges of the entire device and insulate all the exposed wires before the electrical characterization.

The conductivity of the tap water was measured by an Orion Star A322 conductivity meter coupled with an Orion 013016MD 2-electrode conductivity cell. The open-circuit voltage (V_{oc}) was measured using an oscilloscope (Tektronix MDO4000C) equipped with a probe (P2220) of high-impedance (10 MΩ). The sampling rate is 10,000 times per second. This sampling rate should be fast enough for this system because no obvious higher voltage values (>5 V) will be measured using a higher sampling rate. Figure 2F shows the measurement results in randomly selected 10 s. The error was calculated based on the fluctuation of the measurement results at least in 100 s. The transferred charge of the sample was measured by a nanocoulomb meter (Monroe model 284) equipped with a 10-nF capacitor.

The output power and the current-voltage characteristic of LEDs were measured by a silicon detector (918D-UV-OD3R) and a precision source/measure unit (Keysight B2902B), respectively.

Cost estimation of the materials in a thin-film droplet-induced electricity generator

As listed in the Experimental Section, the materials employed in a thin-film droplet-induced electricity generator can be categorized into three groups: triboelectric solution and solid films, electric wires, and other subsidiary tapes. For example, a 9-cm^2 droplet generator requires 200-μL liquid PTFE solution,[3] forming a ~2.8-μm-thick layer (Sec. 1 in the supplemental information) with a price of $3.89.[26] However, a 9-$cm^2$

solid PTFE film only costs \$0.028 to \$0.113 (thicknesses ranging from 5 mil to 20 mil),[28] with the potential for further reduction in mass production. This comparison demonstrates the significant economic benefits of the solid PTFE film. For example, if a 10-mil-thick (i.e., ~254 μm) PTFE film is fabricated using the solution-based materials, the cost is \$352.88, which is four orders of magnitude more expensive than that of solid PTFE films. Furthermore, the cost for the remaining materials is low, because the electric wires and tapes are commercially available and commonly used in daily life. For instance, the price is <\$0.01 for one electric wire,[40] <\$0.07 for the 3M double-sided tapes,[41] and <\$0.02 for the copper double-sided tape.[42] Consequently, even accounting for the production losses, the cost of the electric wires and tapes should not exceed \$0.15.

The pulse widths of voltage pulses

In Figure 2F, we selected two additional peaks for analysis, as indicated by the yellow and green arrows in Figure S1A. Both peaks exhibit shapes similar to the one in Figure 2G. Their pulse widths were approximately 28 ms, which were also comparable to the approximately 29 ms width in Figure 2G. The pulse in Figure S1B spanned from 2.942 s to 2.970 s, and the one in Figure S1C ranges from 6.956 s to 6.984 s. Since the pulse width corresponds to the duration of the droplet's contact time with the top Cu electrode, the consistency in pulse widths underscores the stability of the droplet system.

The photograph of the setup to measure the transferred charge

As shown in Figure S2, the charge transfer of the sample was measured by a nanocoulomb meter (Monroe model 284) equipped with a 10-nF capacitor.

Molecular dynamics simulations

Inspired by the pioneering work of ref.[3] that utilized molecular dynamics simulations to confirm charge separation in water and the transition from an open circuit to a closed circuit, we performed analogous simulations to investigate the charge transport and separation in water at the contact with Cu and PTFE. These simulations were conducted using LAMMPS[43] in a canonical ensemble at 300 K controlled by a Nose-Hoover thermostat[44] with a time step of 1 fs. We employed the transferable four-site interaction model TIP4P/Ice[45] and the SHAKE[46] algorithm with a tolerance of 10^{-5} nm for water. The non-bonded interactions were described by Lennard-Jones 6-12 and Coulomb potentials with a cutoff distance of 1 nm ($V(r) = 4\varepsilon_{ij}[(\sigma_{ij}/r_{ij})^{12} - (\sigma_{ij}/r_{ij})^{6}] + q_i q_j/r_{ij}$, where ε_{ij} is the depth of the potential, σ_{ij} is the distance at which the particle-particle potential energy is zero, r_{ij} is the interatomic center-to-center distance, and q_i and q_j are the charges of atoms i and j, respectively[47]). The parameters for PTFE and Cu were taken from ref.[3] and those for the Na^+ and Cl^- ions were taken from ref.[48] The long-range Coulomb interactions were modeled by the particle-particle particle-mesh method with a tolerance of 10^{-3} kcal mol^{-1} nm^{-1}. The Lennard-Jones cross interaction parameters were calculated by the Lorentz-Berthelot rule.

As illustrated in Figure S3, the simulation cell comprised a PTFE film (grey, consisting of two trilayers), a water slab containing Na^+ (purple) and Cl^- (cyan) ions, and top and bottom Cu electrodes (yellow). The dimensions of the simulation cell were 4.35 nm × 6.96 nm × 30.00 nm, with a distance of 4.50 nm between PTFE and the top Cu electrode. The water slab consisted of 4262 water molecules, 44 Na^+ ions, and 44 Cl^- ions. The bottom Cu electrode was placed 10 nm below the PTFE. We assigned 40 negative charges to the middle layer of the top PTFE trilayer and varying numbers of positive charges to the two Cu electrodes with equal spacing to mimic charging of the electrodes. Initially, a 1 ns equilibration was conducted without assigned charges (Figure S3A). Subsequently, a 1 ns switched-off mode simulation[1] was performed with 40 negative charges assigned to PTFE and 40 positive charges assigned to the bottom Cu electrode. Then a 5 ns switched-on mode simulation[1] was performed keeping 40 negative charges on PTFE while shifting the 40 positive charges from the bottom to the top Cu electrode (Figure S3B), which yielded results comparable to ref.[3]: The Na^+ and Cl^- ions (originally homogeneously distributed in the water; Figure S3A) separated to the PTFE/water and Cu/water interfaces, respectively. Subsequently, the variation of the PTFE film thickness was modelled by 5 ns switched-on mode simulations with 30 positive charges assigned to the top Cu electrode and 10 positive charges assigned to the bottom Cu electrode (Figure S3C) as well as 10 positive charges assigned to the top Cu electrode and 30 positive charges assigned to the bottom Cu electrode (Figure S3D). Despite the different charges on the two Cu electrodes, the separation of the Na^+ and Cl^- ions persisted (ensuring a closed circuit) although with less ions participating.

LEDs with small turn-on voltages

Here we show a list of turn-on voltages in Table S1 for reference in selection of LEDs. In particular, DGs exhibit better compatibility with LEDs that possess lower turn-on voltages, e.g. IR LEDs, which show promising potential in domains like IR data transmission,[49] object detection,[50] and illumination for the night-vision surveillance.[51]

The spatial distribution and the optical setup for LEDs

Based on the spatial distribution depicted in Figure S4A, the LED emits directional light, strongest vertically upwards and gradually diminishing as it approaches the horizontal plane. To ensure a fair comparison of LED intensities (highlighted by a cyan circle), an optical setup has been incorporated in Figure S4B to orient the LEDs upwards. Figure S4C presents the detailed profile of the optical setup following the yellow dotted curve in Figure S4B. Foam blocks were utilized to elevate the mounting base (BA1 from Thorlabs), ensuring the LED's insulation cap aligns perfectly with the top surface of the base.

The voltages and light intensities of the nine LEDs

To further analyze the brightness of the nine LEDs (i.e., LED4∼LED12) in Figure 3F quantitatively, we convert this color image (i.e., Figure 3F) into a grayscale format (Figure S5) to extract the light intensity (i.e., the sum of luminance in Matlab) from each LED within defined rectangular regions.

The extracted light intensities and the voltage values of the nine LEDs are detailed in Table S2. The voltages and light intensities fluctuated in the range of 1.00% and 18.29% (i.e., coefficient of variation), respectively.

The uniformity of LEDs in previous demonstrations

To assess the uniformity of the LEDs, we compared the intensities of the LEDs from Video S1 in ref.[3] (Figure S6A), and Video S3 in ref.[4] (Figure S6B), respectively. Initially, three color frames were extracted from each video (left panel) and subsequently converted into grayscale representations (center panel). Within these grayscale images, two specific LEDs were highlighted, as indicated by the rectangles. Given that LEDs produce directional light, we intentionally chose neighboring LEDs, to rule out the light intensity difference due to focus, with analogous emission directions, evidenced by the similarities in light pattern shapes and sizes. Nonetheless, due to the inability to ascertain the precise configuration of the LED directions in the videos, we cannot entirely rule out the possibility for varied emission directions among the selected LEDs. The cumulative luminance inside the rectangles from the grayscale images was then computed for comparison (right panel with corresponding color). Notable uniformity discrepancies were discernible both visually (left and center panels) and through quantitative analysis (right panel), as presented in Figure S6.

The voltages and light intensities of the remaining six LEDs

After excluding LED4, LED6 and LED12, the voltage redistribution lead to augmented light intensities. Therefore, two polarizers (LPVISE100-A from Thorlabs) were utilized to attenuate this heightened intensity, ensuring that the light did not reach saturation. For further quantitative analysis, we extract the light intensity of each LED from the grayscale representation in Figure S7.

The extracted light intensities and the voltage values of the remaining six LEDs in Table S3. The improved voltages and light intensities fluctuated in the range of 0.67% and 3.10% (i.e., coefficient of variation), respectively.

The current-voltage characteristics of ten LEDs

Ten LEDs from the LED array depicted in Figure 4 were selected at random for uniformity inspection. As shown in Figure S8, the current-voltage characteristics of these ten LEDs exhibited reasonably uniform. Therefore, the LED array in Figure 4 could produce uniform light patterns.